J. Fluid Mech. (2002), *vol.* 462, *pp.* 31–42. © 2002 Cambridge University Press
DOI: 10.1017/S0022112002008200 Printed in the United Kingdom

The structure of an unstable circular vortex in a background straining flow

By KEITH HIGGINS, ANDREW OOI
AND M. S. CHONG

Department of Mechanical Engineering, The University of Melbourne, Victoria 3010, Australia

(Received 4 October 2001 and in revised form 17 January 2002)

The formation of compound vortices from a 'shielded' vortex monopole embedded in a two-dimensional background straining flow is studied numerically. The computations are performed in plane polar coordinates using an infinite radial domain Navier–Stokes solver. The straining flow excites an azimuthal instability, leading to vortex tripole formation in the case of small strain rates. For larger strain rates, tripole formation proceeds briefly before the structure is destroyed by the dominant background straining flow.

1. Introduction

The formation of compound vortex structures is now a well-known feature of two-dimensional or quasi-geostrophic flows. Coherent vortical structures have been observed in the oceans, the atmosphere and the laboratory. These vortices influence the transport of passive scalars such as heat and biochemical compounds in large-scale geophysical flows. Owing to these important effects, the dynamics of these vortices has been studied extensively over the past two decades (Hopfinger & van Heijst 1993).

Various laboratory experiments have revealed the range of compound vortices that can emerge in a two-dimensional flow due to the growth of instabilities of isolated circular vortices (Carnevale & Kloosterziel 1994). This has provided a rich phenomenology of monopoles, dipoles, tripoles, 'triangular' vortices, and more recently the observation of a 'square' vortex (Kloosterziel & Carnevale 1999). In particular, the development of vortex tripoles has been studied in the laboratory by van Heijst & Kloosterziel (1989), van Heijst, Kloosterziel & Williams (1991) and Kloosterziel & van Heijst (1991). These experiments used dye visualization to show that a stable tripolar structure can emerge from an unstable cyclonic vortex in a rotating fluid. It is now understood that such vortices can appear in quasi-geostrophic flows with initially randomly distributed vorticity fields due to the spectral transfer of kinetic energy to larger scales (McWilliams 1984).

There have been various numerical studies of the formation of compound vortex structures. Carton, Flierl & Polvani (1989) investigated the evolution of a 'shielded' vortex monopole with zero circulation. This vortex consists of a circular core of positive vorticity surrounded by a shielding ring of negative vorticity (henceforth referred to as a shielded vortex). The response of such a vortex to azimuthal perturbations of wavenumber $k = 2$ was found to lead to tripole formation, provided that the initial vorticity gradients were steep enough. Carton & Legras (1994) studied tripole formation from a shielded vortex in greater detail. They demonstrated that the long-time asymmetric breaking of the tripole into a dipole and a monopole is driven by

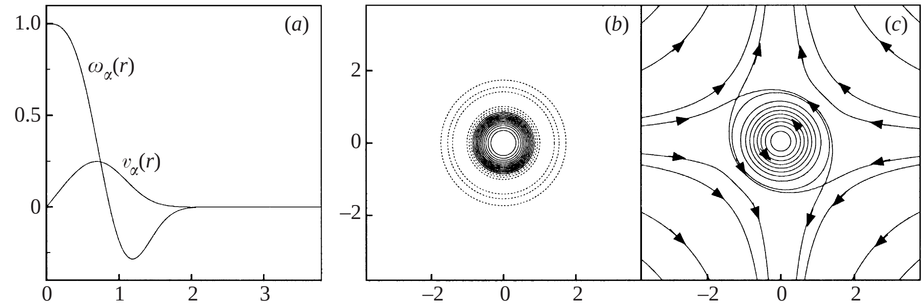

FIGURE 1. Representative initial conditions for $\alpha = 3$, $\beta = 0.005$, $Re = 10\,000$. (*a*) Vorticity and azimuthal velocity profiles. (*b*) Vorticity contours, where dashed contours indicate negative values. Minimum contour is $\omega_{min} = -0.194$ and the contour interval is $\Delta\omega = 0.078$. (*c*) Streamlines.

the erosion of the vortex core by stripping and diffusion. More recently, Kloosterziel & Carnevale (1999) investigated tripole, ‘triangular’ and ‘square’ vortex formation from shielded vortex monopoles. They derived a finite-dimensional dynamical system which was used to model the evolution of the unstable vortex from a circular to a compound structure. These numerical investigations employed a spectral method on a doubly periodic Cartesian domain, with hyperviscosity used to dissipate fine-scale enstrophy.

The behaviour of isolated stretched vortices and vortex patches in straining flows has been studied extensively (Saffman 1992). A strain field perhaps idealizes the leading-order distortional effect of far-field vortices in a multiple vortex flow. It is well known that background straining flows may deform, erode or destroy two-dimensional vortices (Legras, Dritschel & Caillol 2001 and references therein). The results of such isolated vortex studies have been related to simulations of two-dimensional turbulent flows, with good agreement (Jiménez, Moffatt & Vasco 1996). The dynamics of compound vortical structures embedded in straining flows has received less attention. However, Morel & Carton (1994) used contour surgery to test the stability of multipolar equilibria embedded in a deformation field consisting of rotational and straining flow parts. The multipoles were generated from unstable piecewise-constant vortex monopoles using monochromatic azimuthal perturbations, with zero background strain.

In this paper, we present a numerical study of the evolution of a shielded monopolar vortex embedded in a two-dimensional irrotational biaxial background straining flow. We investigate the effect of a range of strain rates at a single Reynolds number. Our study is focused on the initiation of instability, the formation of compound vortex structures and their intermediate-time evolution. An integrated picture of the unfolding of the instability is presented, rather than an investigation of possible long-time steady states.

2. Two-dimensional isolated circular vortices

2.1. *Initial vorticity profile*

Carton & Legras (1994) and Kloosterziel & Carnevale (1999) investigated the stability of shielded monopolar vortices with an initial vorticity profile of the form

$$\omega_\alpha(r) = \omega_0 \left[1 - \tfrac{1}{2}\alpha \left(\frac{r}{\delta}\right)^\alpha\right] \exp(-(r/\delta)^\alpha), \tag{2.1}$$

where α and ω_0 determine the shape and amplitude of the profile and δ is a reference length scale. The corresponding azimuthal velocity is $v_\alpha(r) = \frac{1}{2}\omega_0 r \exp(-(r/\delta)^\alpha)$, so that the flow is everywhere counter-clockwise. The vorticity and azimuthal velocity profiles are shown in figure 1(*a*) and the vorticity contours in the (x, y)-plane are shown in figure 1(*b*). For $\alpha > 0$, all of the vorticity profiles have an inflection point. These isolated vortices have zero circulation, such that $\int_0^{2\pi}\int_0^{\infty} \omega(r, \theta, t) r \, \mathrm{d}r \, \mathrm{d}\theta = 0$. As a necessary condition for instability, Rayleigh's inflection point theorem requires $\mathrm{d}\omega/\mathrm{d}r$ to change sign somewhere, as demonstrated by Drazin & Reid (1981). For vortices with zero circulation, $\mathrm{d}\omega/\mathrm{d}r$ always changes sign somewhere if ω is continuous. We then define the initial shielding ring radius as

$$r_s = (1 + 2/\alpha)^{1/\alpha}. \tag{2.2}$$

This is the radial location at which $\mathrm{d}\omega/\mathrm{d}r = 0$, corresponding to the position of maximum negative vorticity.

For small enough $\alpha > 0$, these vortices are stable. As α is increased, the vorticity profiles become steeper. Kloosterziel & Carnevale (1999) solved an eigenvalue problem using the method of Gent & McWilliams (1986) to obtain the growth rates of the most unstable azimuthal modes as a function of α. They found that for approximately $\alpha > 1.85$, the shielded vortex first becomes unstable to perturbations of azimuthal wavenumber $k' = 2$. They subjected the shielded vortex given by (2.1) to initial vorticity perturbations of the form

$$\omega'_\alpha(r) = \mu \cos(k'\theta) \exp\left[\frac{-(\alpha(r/\delta)^\alpha - 2)^2}{2\sigma^2}\right], \tag{2.3}$$

where μ and σ are parameters used to adjust the amplitude and distribution of the disturbance. They found that perturbations with $k' = 2$ resulted in the formation of a tripolar vortex.

In this study, we employ the vorticity profile (2.1) with $\alpha = 3$ as the initial condition. In § 4.2 the shielded vortex is subjected to perturbations of the form (2.3) with $\mu = 0.1$, $\sigma = 0.25$ only as a reference scenario in the case of zero background strain.

2.2. *Background straining flow*

In this paper, we embed the shielded vortex in a two-dimensional irrotational biaxial background straining flow given by

$$\boldsymbol{u}_s(x, y) = -\beta x \hat{\boldsymbol{i}} + \beta y \hat{\boldsymbol{j}}. \tag{2.4}$$

Here β is a constant strain rate. On converting to plane polar coordinates the strain field is then

$$\boldsymbol{u}_s(r, \theta) = -\beta r \cos(2\theta)\hat{\boldsymbol{r}} + \beta r \sin(2\theta)\hat{\boldsymbol{\theta}}. \tag{2.5}$$

It is clear from (2.5) that the two-dimensional background straining flow introduces azimuthal wavenumber $k = 2$ velocity variations. The full velocity field $\boldsymbol{u}$ can be written as the sum of the velocities induced by the vortex, $\boldsymbol{v}$, and the background straining flow, $\boldsymbol{u}_s$, as

$$\boldsymbol{u}(r, \theta, t) = \boldsymbol{v}(r, \theta, t) + \boldsymbol{u}_s(r, \theta). \tag{2.6}$$

Figure 1(*c*) shows initial streamlines for the velocity field (2.6) with $\alpha = 3$, $\beta = 0.005$.

2.3. *Scaling*

Following Moffatt, Kida & Ohkitani (1994), we define a reference length scale δ and a reference time scale $1/\omega_0$. Anticipating that, even in the case of biaxial strain, the maximum velocity in the vicinity of the vortex is of order $\delta\omega_0$, we introduce the dimensionless variables

$$r^* = r/\delta, \quad \beta^* = \beta/\omega_0, \quad \psi^* = \psi/(\delta\omega_0). \tag{2.7}$$

A Reynolds number based on the reference length and time scales can then be defined as

$$Re = \delta^2\omega_0/\nu, \tag{2.8}$$

where ν is the kinematic viscosity.

2.4. *Governing equations*

The two-dimensional vortex-induced flow considered has uni-directional vorticity $\boldsymbol{\omega} = \omega(r,\theta)\hat{\boldsymbol{k}}$, such that $\boldsymbol{v} = \boldsymbol{v}(r,\theta)$ is the vortex-induced velocity in the (r,θ)-plane. Upon introducing the dimensionless variables (2.7) and dropping the stars, the vorticity transport equation is then simplified to

$$\frac{\partial\omega}{\partial t} + \nabla\cdot(\boldsymbol{u}\omega) = \frac{1}{Re}\nabla^2\omega, \tag{2.9}$$

where $\boldsymbol{\omega} = \nabla \times \boldsymbol{v}$. All quantities are now considered to be dimensionless. As before, $\boldsymbol{u} = \boldsymbol{v} + \boldsymbol{u}_s$. The fluid is incompressible, so a stream function $\psi(r,\theta,t)$ can be associated with the vortex-induced $\boldsymbol{v}$ motion,

$$\nabla^2\psi = -\omega. \tag{2.10}$$

The velocity field derived from the stream function is then

$$\boldsymbol{v} = \frac{1}{r}\frac{\partial\psi}{\partial\theta}\hat{\boldsymbol{r}} - \frac{\partial\psi}{\partial r}\hat{\boldsymbol{\theta}}. \tag{2.11}$$

3. Numerical solution

We solve (2.9) and (2.10) numerically in plane polar coordinates with an infinite radial domain, subject to the initial and boundary conditions on the vorticity field given by

$$\omega(r,\theta,t=0) = \omega_\alpha(r), \tag{3.1}$$

$$\omega(r\rightarrow\infty,\theta,t)\rightarrow 0, \quad t \geqslant 0. \tag{3.2}$$

Here the initial condition is given by the radial vorticity profile (2.1) with $\alpha = 3$. The hybrid spectral finite-difference method developed by Buntine & Pullin (1989) is employed. We represent ω and ψ as

$$\omega(r,\theta,t) = \sum_{k=-N_\theta/2}^{N_\theta/2-1} \hat{\omega}_k(r,t)\mathrm{e}^{\mathrm{i}k\theta} \quad \text{and} \quad \psi(r,\theta,t) = \sum_{k=-N_\theta/2}^{N_\theta/2-1} \hat{\psi}_k(r,t)\mathrm{e}^{\mathrm{i}k\theta}, \tag{3.3}$$

where $r \in [0,\infty)$, $\theta \in [0,2\pi)$ and N_θ is the azimuthal truncation parameter. Here $\hat{\omega}_{-k} = \overline{\hat{\omega}_k}$ and $\hat{\psi}_{-k} = \overline{\hat{\psi}_k}$, where the overline indicates complex conjugation. Substitution of the truncated Fourier series (3.3) into (2.9) and (2.10) yields evolution equations for the Fourier coefficients $\hat{\psi}_k$ and $\hat{\omega}_k$, where $k = -\frac{1}{2}N_\theta \ldots \frac{1}{2}N_\theta - 1$.

There are two steps involved in the calculation: the solution of the Poisson equation and time advancement. The Poisson equation (2.10) gives N_θ linear ordinary differential equations in r for the Fourier coefficients $\hat{\psi}_k$. These were solved on the domain $[0, 1)$ obtained by an algebraic coordinate mapping

$$r = L\zeta/(1-\zeta), \tag{3.4}$$

which maps $r \in [0, \infty)$ onto $\zeta \in [0, 1)$, where L is a stretching parameter. This is different to the trigonometric mapping used by Buntine & Pullin (1989). The stretched equations were solved numerically using fourth-order finite differences at N_r radial nodes, where r-derivatives are related to ζ-derivatives on the uniform grid by appropriate metrics. The boundary condition $\hat{\psi}_k(\zeta \to 1, t) = 0$ was employed. For a detailed discussion of the boundary conditions on $\hat{\psi}_k(\zeta = 0, t)$, the reader is referred to § 2 of Buntine & Pullin (1989). Once the $\hat{\psi}_k$ are known, the non-axisymmetric velocity field is constructed using (2.11). Then, using the vorticity transport equation (2.9), the $\hat{\omega}_k$ were advanced in time using a predictor-corrector scheme. The asymptotic results of Robinson & Saffman (1984) for a Burgers vortex embedded in a non-symmetric strain field were used to validate the code.

4. Results and discussion

4.1. *Vorticity contours and streamlines*

Figures 2 and 3 show the evolution of the vorticity contours and streamlines for the shielded vortex (2.1) with $\alpha = 3$ and $Re = 10\,000$, for background strain rates in the range $0.005 \leqslant \beta \leqslant 0.050$. In all cases, $N_r = 256$, $N_\theta = 512$, $L = 1.0$ and the time step $\Delta t = 0.01$.

Figure 2(a) shows that for $\beta = 0.005$, the azimuthal wavenumber-2 velocity variations provided by the background strain field cause the initially circular vortex to develop into a tripolar vortex. The corresponding streamlines are shown in figure 2(b). The initial streamlines resemble a cat's-eye structure, in which positive and negative vorticity is confined to an interior region of nearly circular streamlines between the two stagnation points. Since the stagnation points on the separatrices penetrate the shielding ring, some negative vorticity exists outside the cat's eye. We then expect that in addition to viscous diffusion, some erosion of the negative vorticity will result from the passive transport of vorticity by the background strain field. Initially, the emerging tripole satellites are aligned with the y-axis, the axis of maximum extensional strain. At $t = 40$, the streamlines show the presence of four saddles. Two of these are connected with separatrices encircling the vortex core, forming a distorted cat's eye. As the negative-vorticity satellites emerge, they entrain positive-vorticity from the core. A large elliptical deformation of the positive-vorticity core is evident at $t = 60$ and by $t = 80$ filamentary spiral arms appear. The tripole then exhibits oscillations (not shown), in which the spiral arms are shed from the core. These arms are stretched by a combination of the background strain and interactions with the satellites. Parts of the arms rejoin the core, but some portions of them cross the cat's-eye separatrix, are transported away by the strain and are subsequently diffused. These features are very similar to those of the tripoles in the numerical simulations of Carton & Legras (1994) and Kloosterziel & Carnevale (1999).

The number of orbits executed by the satellites, N_O is shown on the frames in figure 2(a). By time $t = 300$, 2.34 orbits of the core have been completed. As pointed out by a referee, this represents only a few units of the characteristic inertial time for the tripolar vortex. The maximum vorticity $\omega_{max}(t)$ at $r = 0$ is also shown on

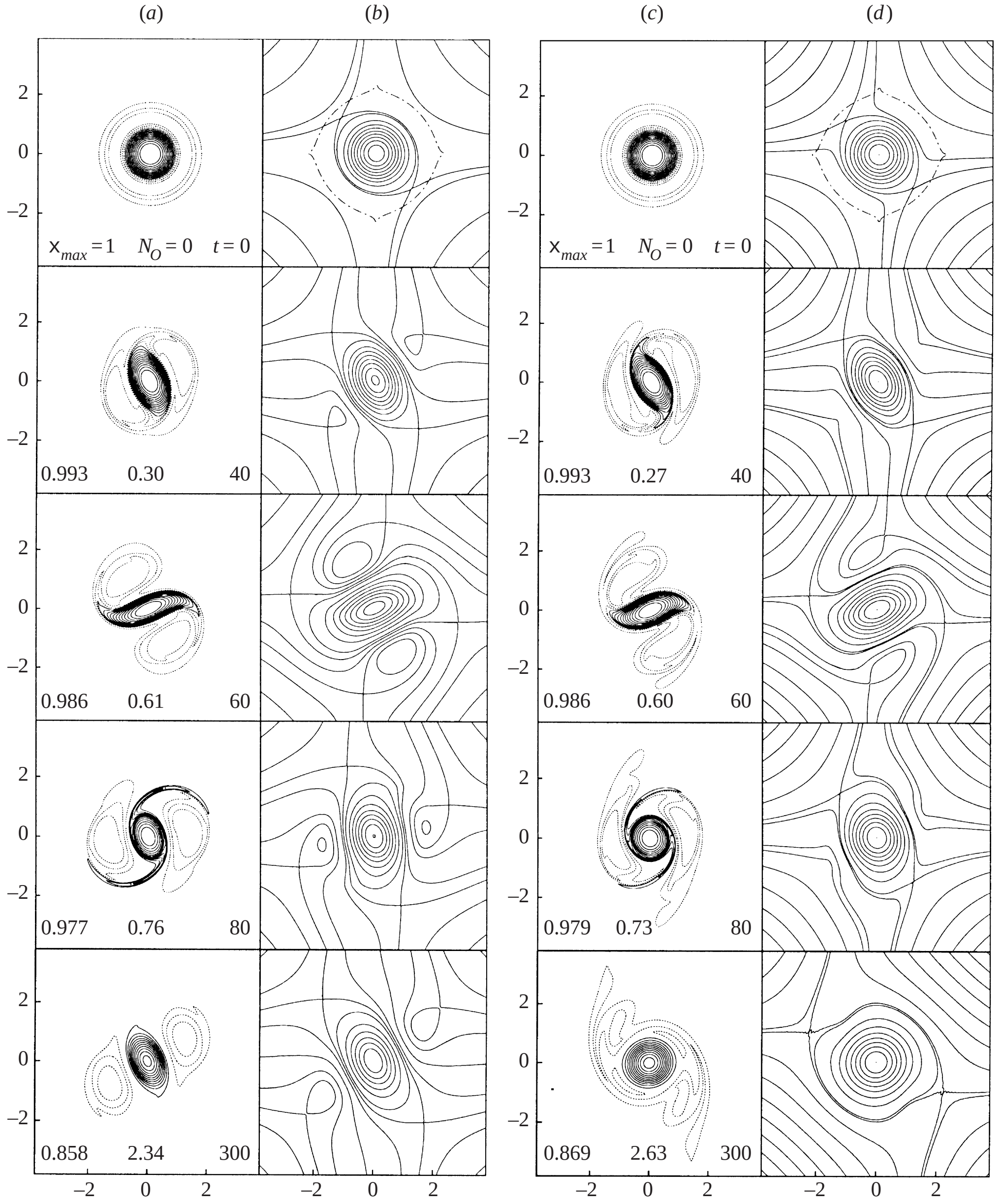

FIGURE 2. Evolution of a shielded vortex with $\alpha = 3$ and $Re = 10\,000$. Contours of vorticity and stream function for (a,b) $\beta = 0.005$, (c,d) $\beta = 0.010$. Vorticity contour levels are the same as in figure 1(b). Radial grid spacing in the frames varies between $\Delta r_{min} = 0.004$ and $\Delta r_{max} = 0.149$. The chain dashed curves on the initial streamline plots indicate the radial positions where the azimuthal velocity is within $\pm 5\%$ of the azimuthal component of the imposed strain field. ω_{max} is the vorticity at $r = 0$ and N_O is the number of orbits executed by the satellites.

the frames. Initially, $\omega_{max}(0) = 1$ and the value at later times provides a measure of the erosion of the positive-vorticity core. As noted by Carton & Legras (1994), the core is continuously and irreversibly eroded during each cycle of spiral arm shedding. By $t = 300$, the maximum vorticity has decreased to $\omega_{max} = 0.858$. For comparison, a purely diffusive simulation in the absence of a background straining flow and instability (not shown) gives $\omega_{max} = 0.880$ by $t = 300$. This erosion must continue in the absence of a vorticity-intensifying stretching strain. The combined effect of the core erosion and the passive transport of negative vorticity from the tripole may lead to different long-time behaviour. Therefore, the tripole structure at $t = 300$ should be viewed as an intermediate-time state.

Figure 2(c, d) shows the evolution of the shielded vortex for $\beta = 0.010$. The increase in streamline density indicates that the background straining flow is becoming more dominant. However, tripole formation proceeds and by $t = 60$ the positive vortex core is surrounded by two satellites. At $t = 80$, these satellites are much deformed in shape compared to the $\beta = 0.005$ satellites at the same time. The filamentary spiral arms are also shorter in length and smaller in vorticity magnitude. By $t = 300$, the vortex core is slightly less eroded than it was at the same time in the $\beta = 0.005$ simulation. The satellites have partially merged around the core and the saddles associated with the satellites have vanished.

For the larger strain rate $\beta = 0.020$, figure 3(a, b) shows that the stagnation points penetrate the shielding ring of vorticity further. Tripole formation proceeds briefly, but before the satellites can properly form, they become elongated and are transported away by the background strain. The combined effect of the strain and the wind-up of the satellites by the core causes the negative vorticity contours to be folded into a complex structure. By $t = 200$, the strain has stripped away most of the negative vorticity, leaving a core which is confined to the cat's eye. The streamlines retain the cat's-eye structure throughout the evolution, although they are distorted at intermediate times.

The largest strain case, $\beta = 0.050$ is shown in figure 3(c, d). Here most of the initial negative vorticity lies outside the cat's eye. The strong strain suppresses tripole formation and the stripping of negative vorticity from the shielding ring begins immediately. Spiral arms develop and these move into regions where they are transported away by the action of the strain. By $t = 80$, only the positive-vorticity core and a small residue of negative vorticity remains, while the maximum vorticity decreases to $\omega_{max} = 0.978$. The core is confined to a cat's eye region of elliptical streamlines. This is reminiscent of the results of Prochazka & Pullin (1998), who studied the behaviour of a stretched Burgers vortex in a non-symmetric strain field, parameterized by a strain ratio, λ.

The total circulation in the simulations shown in figures 2 and 3 must remain zero. For the weak strain rates $\beta = 0.005$ and $\beta = 0.010$, any negative vorticity stripped from the shielded vortex was diffused to small values before it could be transported into regions of coarse grid resolution far from the origin. Numerical problems were avoided and the total circulation remained zero. For the stronger strain rates $\beta = 0.020$ and $\beta = 0.050$, stripped vorticity was transported intact into the far field. This caused the calculations to become under-resolved by $t = 200$ and $t = 100$ respectively. Data collection ceased at these times.

4.2. *Flow diagnostics*

Figure 4 shows the time histories of flow diagnostics obtained during the simulations shown in figures 2 and 3. Figure 4(a) shows the evolution of the satellite core separation, $d_c(t)$, which is the distance between the two largest negative values of vorticity in the flow field. All the curves intercept the d_c-axis at $d_c(0) = 2r_s = 2.3713$, where r_s is the initial radius of the shielding ring from (2.2). The evolution of the shielded vortex excited with perturbations given by (2.3), but with zero background strain is shown as a bold line for reference. The bold dotted curve shows the evolution

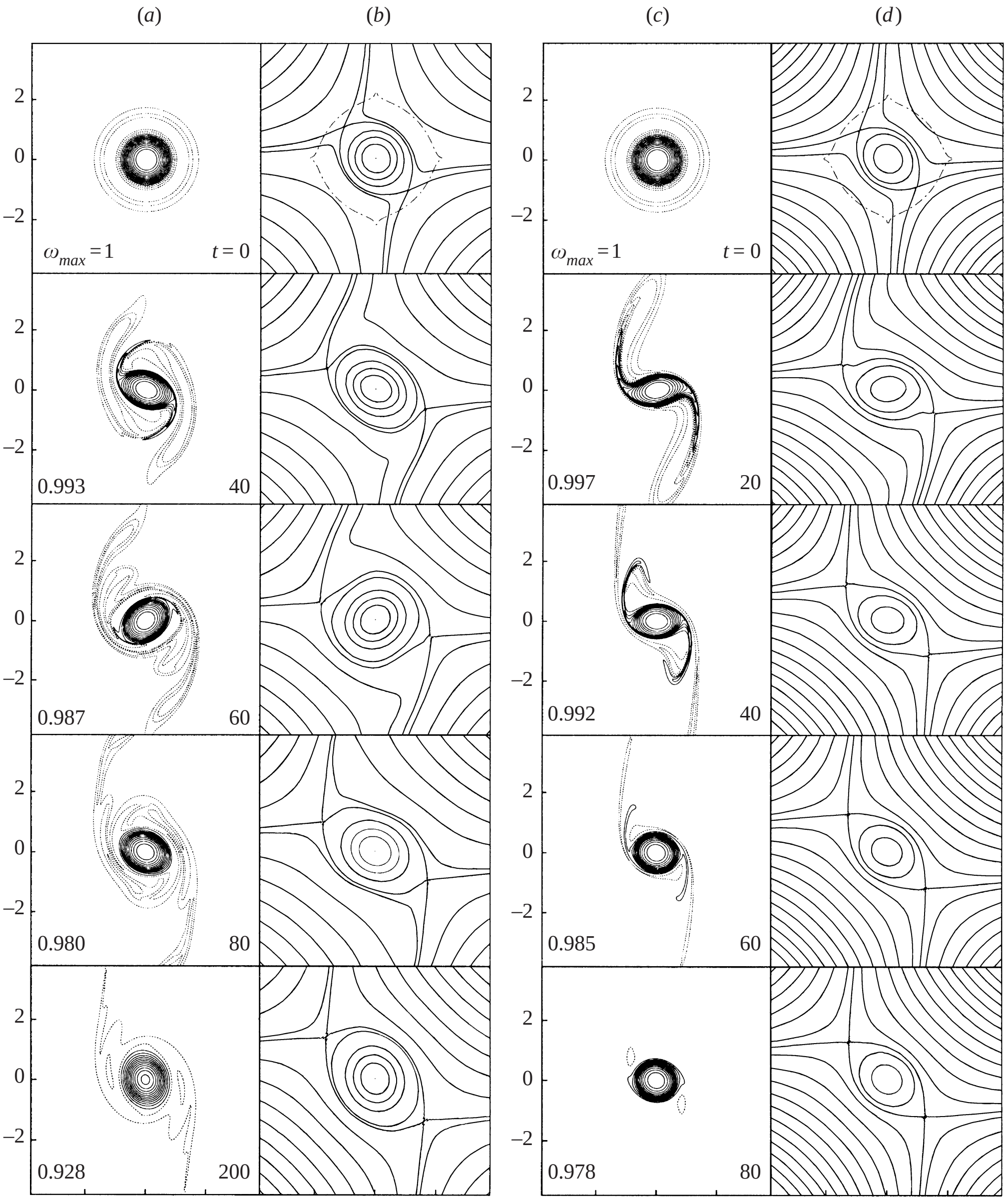

FIGURE 3. Evolution of a shielded vortex with $\alpha = 3$ and $Re = 10\,000$. Contours of vorticity and streamfunction for (a, b) $\beta = 0.020$, (c, d) $\beta = 0.050$. Vorticity contour levels are the same as in figure 1(b). ω_{max} is the vorticity at $r = 0$. See figure 2 for an explanation of the chain dashed curves and radial grid spacing.

of the shielding ring diameter for a purely diffusive simulation, in the absence of strain or any instability.

Comparing the $\beta = 0$ curve to the pure diffusion curve, we see that there is a faster-than-diffusive growth in d_c during the tripole satellite formation process. This ends at approximately $t = 150$ and the d_c growth rate starts to relax to the pure diffusive rate, although small oscillations are caused by the presence of the satellites.

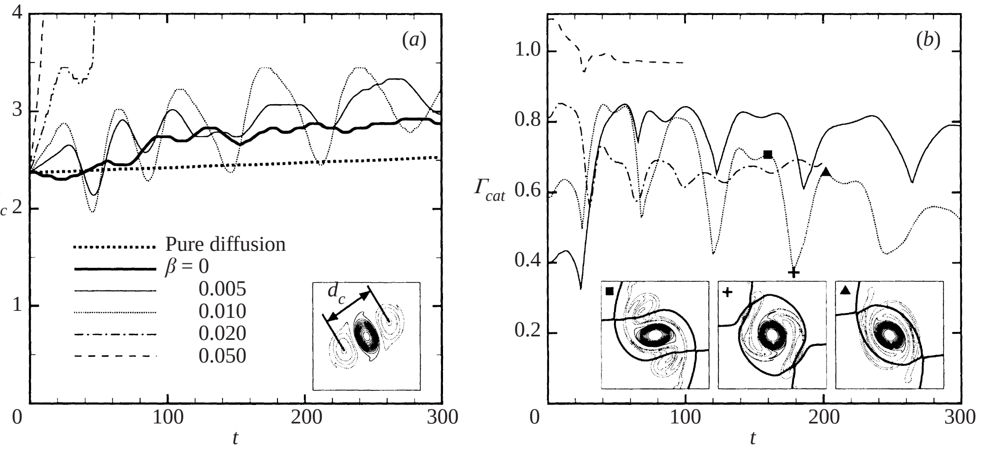

FIGURE 4. Time history of flow diagnostics for $\alpha = 3$ and $Re = 10\,000$. (*a*) Tripole satellite core separation d_c, as defined in the inset. (*b*) Circulation contained in the cat's eye, Γ_{cat}. The insets show the cat's-eye separatrix in bold overlaying the vorticity contours at the times indicated on the $\beta = 0.010$ curve. The initial circulation contained in the positive-vorticity core of the shielded vortex is $\Gamma_+ = 1.2309$. The legend shown in (*a*) applies to both graphs.

For the weak strain cases, we make a similar observation about the initial growth of d_c. Subsequent oscillations are due to the alternating alignment of the satellites with the axes of maximum stretching and contracting strain as they orbit the vortex core. The amplitude of these oscillations grows as the strain rate is increased. However, a faster-than-diffusive d_c growth rate is observed in both cases beyond $t = 150$. The mechanism of this effect is not completely understood. Carton & Legras (1994) showed that the transport of positive-vorticity filaments away from the core of a tripole and their subsequent diffusion leads to an increase in d_c through conservation of angular momentum. Perhaps this effect, combined with or enhanced by the passive transport of vorticity by the background strain field, is responsible for our faster-than-diffusive observation. If this effect persists in the case of weak strain, then the satellites would begin to move into regions of coarse grid resolution. This would lead to under-resolved calculations and a search for long-time steady states would be difficult. For the stronger strain rates $\beta = 0.020$ and $\beta = 0.050$, the negative-vorticity shielding ring is so rapidly stripped away by the background strain that distinct tripole satellite cores are no longer identifiable beyond $t = 50$.

Figure 4(*b*) shows the circulation contained within the cat's eye, Γ_{cat}, obtained by integrating the vorticity field over the region bounded by the cat's-eye separatrix. The initial Γ_{cat} is determined by the depth to which the stagnation points on the cat's-eye separatrix penetrate the shielding ring. Increasing the strain rate excludes more negative vorticity from the cat's eye. The initial circulation contained in the positive-vorticity core of the shielded vortex is $\Gamma_+ = 1.2309$.

For the strain rates $\beta = 0.005$ and $\beta = 0.010$, a large increase in Γ_{cat} begins around $t = 25$. This is related to the elliptical deformation of the core, the onset of mode-2 instability and the transfer of negative vorticity from the cat's eye into the satellites. Γ_{cat} peaks around $t = 60$, when tripole satellite formation is complete. Subsequent oscillations in the Γ_{cat} curves are caused by the flux of vorticity into and out of the cat's eye. This is due to the time variation of both the spatial vorticity distribution and the shape of the cat's eye. These effects are most clearly shown in the insets of figure 4(b) for $\beta = 0.010$. As the strain stretches the satellites, they begin to elongate into arms. The positive core winds up the negative-vorticity arms, entraining them into the cat's eye. The insets show that the cat's-eye separatrix changes shape and area as the arms are wound up, resulting in a decrease in the circulation contained within. As the spiral arms begin to merge around the core, the cat's eye changes shape again and expels some negative vorticity, resulting in an increase in Γ_{cat}. Figure 2 shows positive-vorticity spiral arms crossing the cat's-eye separatrix. This phenomenon also contributes to the time-varying vorticity flux, since the spiral arms are partially entrained back into the cat's eye at later times. The cycle described above is repeated, although the maximum amplitude of Γ_{cat} decreases with time. This decay is due to viscous diffusion and the transport of vorticity across the stagnation points by the background straining flow.

For the larger strain rates $\beta = 0.020$ and $\beta = 0.050$, the shielding ring is rapidly stripped away. Smaller oscillations in the value of Γ_{cat} result from a reduction in the initial negative vorticity contained within the cat's eye and less distortion of the cat's-eye separatrix.

A convenient measure of the amplitude of the Fourier coefficients $\hat{\omega}_k$ from the first of (3.3) is $A_k(t)$, where

$$A_k^2(t) = 2\pi \int_0^\infty \hat{\omega}_k(r,t)\,\overline{\hat{\omega}_k(r,t)}\,r\,\mathrm{d}r. \tag{4.1}$$

Figure 5(a) shows the evolution of the mean and azimuthal components of A_k for the shielded vortex excited with perturbations given by (2.3), but with zero background strain. This corresponds to the bold line in figure 4(a). Here 'mean' indicates the axisymmetric mode $k = 0$ and 'azimuthal' indicates the sum of the non-axisymmetric modes $k \geqslant 1$. After some initial delay, there is a rapid increase in the amplitude of the azimuthal component, associated with the emergence of fine scales. This component is only larger in amplitude than the mean for a short time. Oscillations in the amplitudes of both components subsequently decay. Figure 5(b) shows the evolution of the two components for $\beta = 0.005$. In this case, the biaxial strain field initiates the instability. Here more dynamical behaviour is observed, since the amplitude of the oscillations in the azimuthal part do not decay. The insets show the spatial vorticity distribution at representative local minima and maxima in the amplitude of the azimuthal component. For the minima and maxima, the satellites are aligned with the axes of maximum contracting and stretching strain respectively. At the maxima, the satellites are less elliptical in shape compared to those of the minima and a larger elliptical deformation of the core is evident. A local maximum in the azimuthal component results, since the vorticity field is more non-axisymmetric at this time.

5. Conclusions

We have numerically studied the formation of compound vortices from a shielded vortex embedded in a two-dimensional straining flow for strain rates in the range $0.005 \leqslant \beta \leqslant 0.050$, at $Re = 10\,000$. The strain field provides an azimuthal wavenumber-2 velocity variation which excites an instability leading to vortex tripole formation for small β. Diffusion and the passive transport of vorticity by the background strain field constantly erode the tripole. This may cause different long-time tripole behaviour, so the present results should be viewed as intermediate-time states. For large β, nearly complete stripping of the negative-vorticity shielding ring is observed, resulting in a compact positive vortex in the case $\beta = 0.050$.

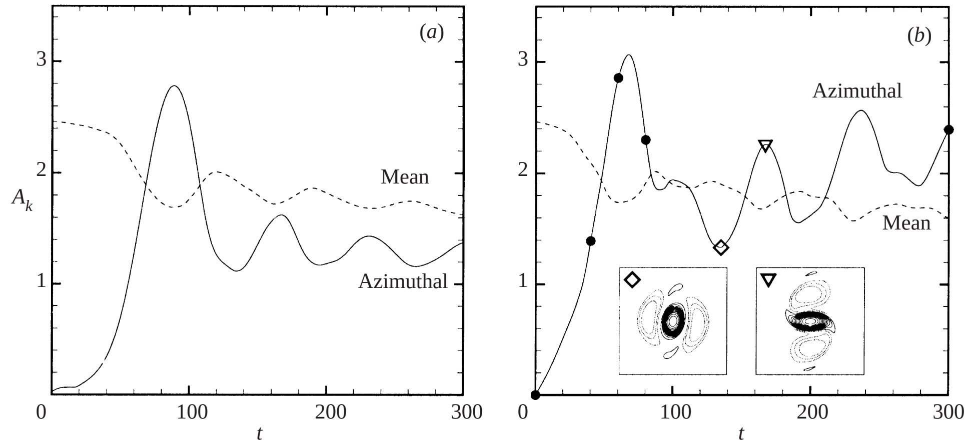

Figure 5. Evolution of the amplitudes of the modes A_k for $\alpha = 3$ and $Re = 10\,000$. (*a*) $\beta = 0$, with instability excited with a vorticity perturbation described by (2.3). Modes A_2 and A_4 account for 43% and 13% of the azimuthal curve respectively at the time of the first peak, $t = 87$. (*b*) $\beta = 0.005$. The solid circles on the azimuthal curve represent the times at which vorticity contours and stream function were shown in figure 2(*a*, *b*). The insets show the vorticity contours at the times indicated by the open diamond and triangle. Modes A_2 and A_4 account for 42% and 12% of the azimuthal curve respectively at the time of the first peak, $t = 72$.

When $\beta \leqslant 0.010$, the amplitude of oscillations in the core separation between the tripole satellites becomes larger with increasing strain rate. Comparison with a purely diffusive simulation shows that the tripole satellite core separation grows at a faster-than-diffusive rate. The streamline patterns retain a cat's-eye structure during the evolution for all the strain rates investigated. A study of the time history of circulation contained within the cat's eye reveals a time-varying flux of vorticity into and out of the cat's eye. This is due to the time dependence of the spatial vorticity distribution and cat's-eye shape. Finally, the vorticity field is found to be more non-axisymmetric when the tripole satellites are aligned with the axis of maximum extensional strain rate.

Support from the Australian Research Council and the Victorian Partnership for Advanced Computing (VPAC) is gratefully acknowledged.

REFERENCES

Buntine, J. D. & Pullin, D. I. 1989 Merger and cancellation of strained vortices. *J. Fluid Mech.* **205**, 263–295.

Carnevale, G. F. & Kloosterziel, R. C. 1994 Emergence and evolution of triangular vortices. *J. Fluid Mech.* **259**, 305–331.

Carton, X. J., Flierl, G. R. & Polvani, L. M. 1989 The generation of tripoles from unstable axisymmetric isolated vortex structures. *Europhys. Lett.* **9**, 339–344.

Carton, X. & Legras, B. 1994 The life-cycle of tripoles in two-dimensional incompressible flows. *J. Fluid Mech.* **267**, 53–82.

Drazin, P. G. & Reid, W. H. 1981 *Hydrodynamic Stability*. Cambridge University Press.

Gent, P. R. & McWilliams, J. C. 1986 The instability of barotropic circular vortices. *Geophys. Astrophys. Fluid Dyn.* **35**, 209-233.

van Heijst, G. J. F. & Kloosterziel, R. C. 1989 Tripolar vortices in a rotating fluid. *Nature* **338**, 569–571.

van Heijst, G. J. F., Kloosterziel, R. C. & Williams, C. W. M. 1991 Laboratory experiments on the tripolar vortex in a rotating fluid. *J. Fluid Mech.* **225**, 301–331.

Hopfinger, E. J. & van Heijst, G. J. F. 1993 Vortices in rotating fluids *Annu. Rev. Fluid Mech.* **25**, 241–289.

Jiménez, J., Moffatt, H. K. & Vasco, C. 1996 The structure of the vortices in freely decaying two-dimensional turbulence. *J. Fluid Mech.* **313**, 209–222.

Kloosterziel, R. C. & Carnevale, G. F. 1999 On the evolution and saturation of instabilities of two-dimensional isolated circular vortices. *J. Fluid Mech.* **388**, 217–257.

Kloosterziel, R. C. & van Heijst, G. J. F. 1991 An experimental study of unstable barotropic vortices in a rotating fluid. *J. Fluid Mech.* **223**, 1–24.

Legras, B., Dritschel, D. G. & Caillol, P. 2001 The erosion of a distributed two-dimensional vortex in a background straining flow. *J. Fluid Mech.* **441**, 369–398

McWilliams, J. C. 1984 The emergence of isolated coherent vortices in turbulent flow. *J. Fluid Mech.* **146**, 21–43.

Moffatt, H. K., Kida, S. & Ohkitani, K. 1994 Stretched vortices – the sinews of turbulence; large-Reynolds number asymptotics *J. Fluid Mech.* **259**, 241–264.

Morel, Y. G. & Carton, X. J. 1994 Multipolar vortices in two-dimensional incompressible flows. *J. Fluid Mech.* **267**, 23–51.

Prochazka, A. & Pullin, D. I. 1998 Structure and stability of non-symmetric Burgers vortices. *J. Fluid Mech.* **363**, 199–228.

Robinson, A. C. & Saffman, P. G. 1984 Stability and structure of stretched vortices. *Stud. Appl. Maths* **70**, 163–181.

Saffman, P. G. 1992 *Vortex Dynamics*. Cambridge University Press.